Journal of Materials Chemistry A

ROYAL SOCIETY OF CHEMISTRY

PAPER

View Article Online
View Journal | View Issue

Cite this: J. Mater. Chem. A, 2025, 13, 38140

The case against hole injection through SAMs in perovskite solar cells

Fraser J. Angus, †[a] Lewis Mackenzie, †[a] Marcin Giza, [a] Dylan Wilkinson, [a] Elisabetta Arca, [b] Emilio Palomares, [cd] Wenhui Li, *[c] Pablo Docampo *[ae] and Graeme Cooke *[a]

Self-assembled molecules (SAMs) are widely used as hole-selective contacts in perovskite solar cells (PSCs). They are traditionally designed to facilitate charge injection by aligning their highest occupied molecular orbital (HOMO) with the perovskite's valence band. However, interfacial energy barriers may not necessarily hinder performance, and in some cases, can boost the devices' open-circuit voltage, thereby improving efficiency. This raises an important question: is injection through the SAM, to promote charge extraction, a necessary or even desirable criterion? To investigate this, we compare two Spiro-OMeTAD derivatives: **Spiro-A**, which is directly attached to the indium-doped tin oxide (ITO) anode by a carboxylic acid moiety, forcing the HOMO level to be in close proximity to the ITO, and **Spiro-B**, which incorporates a spacer group to separate the HOMO from ITO spatially. Contrary to expectations, **Spiro-B** achieves a higher open-circuit voltage (V_{OC}) and power conversion efficiency (PCE) than **Spiro-A** despite having a lower built-in potential (V_{BI}). Stabilise and pulse (SaP) measurements confirm that **Spiro-B** promotes charge accumulation by reducing interfacial recombination, thus increasing quasi-Fermi level splitting (QFLS). Furthermore, the carbazole-based reference SAM (**Me-4PACz**) achieves the highest V_{OC}, demonstrating that direct charge injection is not always beneficial. These results challenge conventional molecular design strategies, emphasising the importance of controlling interfacial recombination over maximising charge injection. This work provides new insights for optimising SAMs in PSCs, offering a pathway toward higher efficiency through tailored energy barriers and charge accumulation dynamics.

Received 19th August 2025
Accepted 1st October 2025

DOI: 10.1039/d5ta06749a

rsc.li/materials-a

Introduction

Perovskite solar cells (PSCs) have emerged as a leading photovoltaic technology, boasting exceptional power conversion efficiencies (PCE) and the potential for low-cost fabrication.[1,2] A critical aspect of PSC performance lies in designing and optimising interfacial layers that mediate charge extraction and transport.[3] Self-assembled molecules (SAMs) have attracted significant attention as interfacial modifiers,[4] this is due to their ability to tailor energy-level alignment,[5] reduce interfacial defects,[6] and enhance device stability.[7]

When designing SAMs, two key parameters need to be considered. The first is the strength of the dipole and its effect on the underlying charge extraction electrode.[8–10] The second is the alignment of the Highest Occupied Molecular Orbital (HOMO) with the perovskite's valence band (VB) energy level. This alignment is typically optimised to facilitate charge extraction and minimise charge build-up.[11] However, the dipole of the SAM can introduce energetic offsets at the interface between the charge extraction contact and the perovskite.[12,13] In previous work, we have shown that for carbazole-based SAMs, such as (4-(3,6-dimethyl-9*H*-carbazol-9-yl)butyl)phosphonic acid (**Me-4PACz**), this can lead to an interfacial energy barrier.[14] This, in turn, leads to the accumulation of photogenerated charge at the interface, resulting in a wider quasi-Fermi level splitting (QFLS) and thus boosting open-circuit voltage (V_{OC}).[14] These devices also show an improvement in PCE, as carbazole-based SAMs are very effective at suppressing interfacial recombination.[11,15,16] This finding highlights that, contrary to conventional expectations, an interfacial energy barrier is not necessarily detrimental to device performance.

The design criteria of SAMs for use in PSCs have drawn heavily from the advancements made in dye design for dye-sensitised solar cells (DSSCs).[17] Here, the most effective dyes

[a]School of Chemistry, University of Glasgow, Glasgow G12 8QQ, UK. E-mail: Graeme.Cooke@glasgow.ac.uk
[b]School of Mathematics, Statistics and Physics, Newcastle University, Newcastle upon Tyne, NE1 7RU, UK
[c]Institute of Chemical Research of Catalonia (ICIQ-CERCA), 43007 Tarragona, Spain. E-mail: wli@iciq.es
[d]Catalan Institution for Research and Advanced Studies (ICREA), 08010 Barcelona, Spain
[e]Basque Center for Materials, Applications and Nanostructures (BCMaterials), 48940 Leioa, Spain. E-mail: Pablo.Docampo@bcmaterials.net
† Authors contributed equally.

incorporated both an energetically favourable transition and a molecular orbital overlap with the charge extraction electrode.[18] This promotes ultrafast charge extraction from the dyes, as the rapid electron transfer outcompetes recombination processes, enabling high photogenerated current densities and maximising performance.[19–21]

We have recently reported a SAM (**Spiro-A**) synthesised by the mono-demethylation of commercially available Spiro-OMeTAD, which features a carboxylic acid anchoring group.[22] This material is a classic example of following traditional design paradigms, where the HOMO overlaps with the charge extraction electrode. The resulting device showed efficiency comparable to that of a poly[bis(4-phenyl)(2,4,6-trimethylphenyl)amine] (PTAA)-based device; however, it did not outperform competing carbazole-based SAM layers. This raises an important question: is injection through the SAM, to promote charge extraction, a necessary or even desirable criterion?

In this work, we address this question by investigating the relationship between SAM structure and device performance metrics. We have developed a novel SAM, **Spiro-B**, which includes a spacer group in the form of a hexyl alkyl chain, ensuring there is a spatial gap between the HOMO and the anode when incorporated in solar cells. Both Spiro moieties are compared against a carbazole-based reference SAM (**Me-4PACz**). We hypothesise that **Spiro-A** promotes efficient charge injection with a direct HOMO-valence band overlap at the interface. In contrast, **Spiro-B**, lacking this overlap, may cause charge accumulation at the interface.

To disentangle these relationships, we employ a combination of spectroscopic and electronic characterisation techniques, including X-ray photoelectron spectroscopy (XPS), time-resolved photoluminescence (TRPL) and stabilise and pulse (SaP) measurements. Standard current density–voltage (*J–V*) scans reveal that **Spiro-B** achieves a higher V_{OC} and overall PCE than **Spiro-A**, whilst **Me-4PACz** delivers the best performance overall. Moreover, SaP measurements indicate that the **Spiro-B** derivative leads to a reduction in the built-in potential (V_{BI}) compared to **Spiro-A**, yet it still demonstrates better performance. We note that both are outperformed by the carbazole derivative, highlighting that promoting charge extraction in PSCs is not necessarily a driver of higher performance, thus challenging conventional molecular design criteria.

Experimental methods

Solar cell fabrication

The patterned ITO substrates (1.5 cm × 1.5 cm, 15 Ω sq^{-1}) were sequentially cleaned with ethanol and IPA for 30 minutes. Then, the ITO substrates were treated with UV-O_3 for 30 min before being transferred to an N_2 glovebox. **Spiro-A** and **Spiro-B** SAMs were dissolved in DMF at a concentration of 0.1 mM, respectively. **Me-4PACz** was dissolved in ethanol with a concentration of 0.1 mM. The SAM solutions were spin-coated on ITO substrates at 3000 rpm for 60 s and then annealed at 100 °C for 10 min. After cooling to room temperature, the perovskite solution was spin-coated onto the SAM at 2000 rpm for 10 s and 4500 rpm for 25 s. 200 μL of chlorobenzene was dropped on the spinning substrate with 12 s remaining. The samples were then annealed at 100 °C for 30 min. The perovskite solution with a concentration of 1.5 M was prepared by mixing FAI, PbI_2, MABr and $PbBr_2$ in DMF : DMSO mixed solvent (4 : 1 v/v). CsI in DMSO solution (1.5 M) was added to the perovskite precursor to form the final perovskite solution with the chemical formula of $Cs_{0.05}(FA_{0.95}MA_{0.05})_{0.95}Pb(I_{0.95}Br_{0.05})_3$ (with 10 mol% MACl). After that, an electron transport layer of $PC_{61}BM$ was deposited from a chlorobenzene solution (20 mg mL^{-1}) at 1000 rpm for 60 s, and then a bathocuproine (BCP) solution (0.5 mg mL^{-1} in isopropanol) was spin-coated on the $PC_{61}BM$ layer at 4000 rpm for 40 s. Finally, a 100 nm Ag layer was evaporated at low pressure (<10^{-6} bar), defining an area of 0.104 cm^2.

Characterisation

UV-Vis absorption was measured in dichloromethane at 10^{-6} mol L^{-1}. Fluorescence emission was measured in dichloromethane at 10^{-7} mol L^{-1} with an excitation wavelength of 391 nm. Cyclic voltammetry was recorded in dichloromethane at a concentration of 10^{-4} mol L^{-1}, scan rate of 0.1 V s^{-1}, with 1 mol L^{-1} tetrabutylammonium hexafluorophosphate as the electrolyte, and referenced to a ferrocenium/ferrocene standard.

The *J–V* curves were recorded using a solar simulator (ABET 11000) and a source meter (Keithley 2400). The curves were measured under 1 Sun conditions (100 mW cm^{-2}, AM 1.5G), calibrated with a Si-reference cell.

XPS spectra were collected on a Kratos Analytical AXIS Supra+, using an Al Kα (1486.6 eV) excitation source. No charge neutraliser was used. Samples were grounded using copper tape to ensure good electrical contact between the sample, the mounting bar and the instrument. Samples were kept in a nitrogen atmosphere during preparation and transferred into the instrument using a purge box directly attached to the instrument to minimise air exposure. The chamber pressure was between 8.3×10^{-8} and 1.3×10^{-7} torr during measurement. Samples were prepared following the same process as was done for solar cell fabrication and, therefore, measured as deposited, with no further treatment.

TRPL spectra were obtained on an Edinburgh Instruments LifeSpec-II apparatus with a 470 nm laser excitation. Excitation was done through the glass/ITO side of the sample. Discussion on the analysis of the data can be found in SI Note 2.

SaP measurements were conducted on a home-built set-up. Measurements were performed using an Ossila Source Measure Unit. The light intensity of the high-power white Cree LED was tuned to match the current output obtained from the calibrated 1 Sun *J–V* measurements. The source delay was set to 10 ms, meaning that the current value acquisition time started approximately 10 milliseconds (ms) after the arrival of the voltage pulse, which is set to the shortest possible length of ~38 ms (set by the USB input). To obtain the current value, the pulse was sampled 256 times, with a sampling time of 14.2 microseconds (μs). This data was averaged out at this rate for 3.62 ms. A stabilisation time of 240–420 seconds was used until a stable current output was obtained. Forward and reverse scans were

done with a 50 mV step voltage. Devices were stabilised for 1 second between each pulse, giving a duty cycle of around 5%.

To extract the electrostatic potential drop across the perovskite for each device, 5 points were taken around the open-circuit voltage, and a 3rd-order polynomial fit was used; the gradient was analysed, giving dJ/dV. The second derivative (d^2J/dV^2) is then used to obtain the steepest gradient. From this obtained point, a range of points above and below this were used to fit multiple linear fits through the steepest section of the raw data to find where the linear fit crosses the midpoint of the maxima and minima of the sigmoid. Multiple linear fits are then made through the range of points to obtain a range of V_{Flat} values. A weighted average calculation, described in ref. 14, is then used to provide the V_{Flat} value. The error associated with this measurement is described in ref. 31.

Results and discussion

Molecular design and electronic properties of spiro SAMs

To investigate how the spatial location of the HOMO level affects charge injection and its subsequent effect on device performance and device metrics, we compare two Spiro derivatives, **Spiro-A** and **Spiro-B**. The previously synthesised **Spiro-A** directly anchors to the indium-doped tin oxide (ITO) electrode through its triphenylamine (TPA) unit *via* a carboxylic acid functional group.[22] In contrast, **Spiro-B** is bonded to a benzoic acid group through a hexyl alkyl chain separator, ensuring a spatial gap between the HOMO of the SAM and the ITO. We also include a reference carbazole-based SAM (**Me-4PACz**) for comparison. The synthetic route for **Spiro-B** is shown in Scheme S1, and full synthetic details are provided in SI Note 1.

The absorption, HOMO energy level, and dipole moment of SAM molecules are all critical parameters to consider when designing these materials. Therefore, we conducted ultraviolet-visible absorption spectroscopy (UV-Vis), fluorescence spectroscopy and cyclic voltammetry (CV). The results from the UV-Vis/fluorescence spectrometry and cyclic voltammetry of **Spiro-B** matched closely with the properties of **Spiro-A** and Spiro-OMeTAD (included as a reference), as shown in Fig. 1. Interestingly, Density Functional Theory (DFT) calculations show that there is a significant difference in the obtained dipole moment: **Spiro-A** has a significant calculated dipole moment of ~8.1 debye (D), whereas **Spiro-B** has a much lower dipole moment of ~2.9 D, as shown in Fig. S12.

Verification of SAM anchoring on ITO substrates

It is essential to demonstrate that these materials are anchored on the ITO surface, as they will be used as the p-type layer in inverted p–i–n perovskite solar cells. To achieve this, we performed XPS measurements after depositing the SAMs. The C 1s spectra of the three samples studied are shown in Fig. S13a–c. Whilst **Spiro-A** shows no additional peaks when compared to the bare ITO, the presence of **Spiro-B** is evident, with the appearance of a distinct C–O peak at 286.3 eV and the aromatic satellite peak at 291.6 eV. The assignments and positions of XPS peaks associated with Spiro-OMeTAD were determined by measuring the XPS of a thin reference film (Fig. S14).

Evidence of SAM attachment to the ITO surface can be most clearly observed in the O 1s spectra, shown in Fig. 2. Here, we observe several peaks associated with the expected ITO species, including bulk indium–oxygen bonds at 530.4 eV, oxygen adjacent to oxygen deficiency sites at 531.2 eV, and surface hydroxy–indium bonds at 532.1 eV.[23] Once the SAM is deposited, we observe the appearance of a peak at 533.1 eV, indicating the presence of the C–O groups of the Spiro moieties. The N 1s spectra, shown in Fig. 2, provides further evidence of SAM deposition, with the ITO reference showing no signal, and the SAM samples containing peaks associated with the Spiro molecule at around 400.1 eV (C–N (a)) and residual dimethylformamide (DMF) solvent at around 400.8 eV (C–N (b)).[24] For complete XPS peak data, see SI Table S1.

To ensure that the SAMs coat the surface uniformly, we performed contact-angle measurements and atomic force microscopy (AFM). The results for a bare ITO sample and a sample using **Spiro-A** and **Spiro-B** are shown in Fig. S15. Here, it was observed that the Spiro SAMs significantly increased the hydrophobicity of the ITO surface compared to bare ITO (from ~30° to ~74°). This indicates successful SAM formation and similar surface wettability between the two Spiro materials. Furthermore, the AFM analysis revealed that the root-mean-square (RMS) roughness remained effectively unchanged upon the SAM deposition, ranging from ~2.83–2.90 nm. These measurements suggest that the Spiro SAMs develop a uniform coat on the surface of the ITO. In combination, these measurements give further evidence that any differences obtained in device performance are due to the electronic properties of the SAMs, rather than differences in perovskite crystallisation.

Device fabrication and photovoltaic performance

Having established from the chemical characterisation (*i.e.* UV-Vis, fluorescence spectroscopy and CV) results that there is a negligible difference energetically between both Spiro moieties and that both can be successfully bound to the ITO surface, we now focus on identifying the link between structure and device metrics. To achieve this, we fabricated PSCs with a device configuration starting with ITO treated with either **Spiro-A**, **Spiro-B** or the reference SAM **Me-4PACz** as the hole-selective layer. The perovskite utilised was an optimised triple cation composition of caesium, formamidinium, and methylammonium ($Cs_{0.05}(FA_{0.95}MA_{0.05})_{0.95}Pb(I_{0.95}Br_{0.05})_3$), followed by [6,6]-phenyl C61 butyric acid methyl ester ($PC_{61}BM$) and bathocuproine as the electron transporting layer and finished with a silver cathode. The whole device fabrication details can be found in the Methods section.

The resulting current density–voltage (J–V) curves, measured under 1 Sun illumination (AM 1.5G, 100 mW cm^{-2}), for the best-performing devices incorporating **Spiro-A**, **Spiro-B** and **Me-4PACz** are shown in Fig. 3a. The **Spiro-A** device achieved a power conversion efficiency (PCE) of 19.7% with a short-circuit current density (J_{SC}) of 23.8 mA cm^{-2}, V_{OC} of 0.99 V and fill factor (FF) of

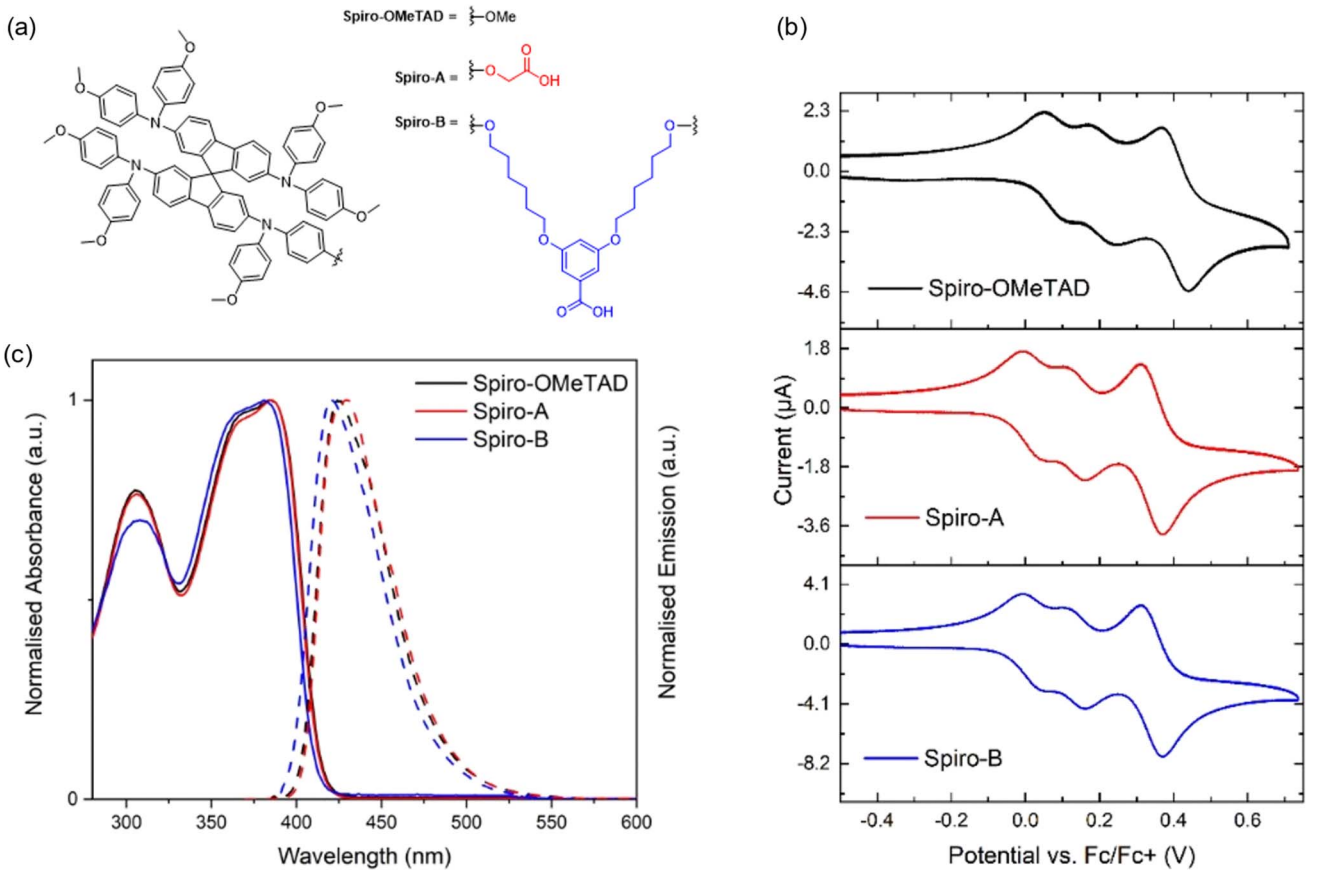

Fig. 1 (a) Molecular structure of **Spiro-A**, **Spiro-B** and Spiro-OMeTAD. (b) Cyclic voltammetry of **Spiro-A**, **Spiro-B** and Spiro-OMeTAD. (c) UV-Vis and fluorescence spectra of **Spiro-A**, **Spiro-B** and Spiro-OMeTAD. Absorbance = solid line, emission = dashed line.

83.9%. Interestingly, the device incorporating **Spiro-B** showed a higher PCE, achieving 20.8% with a J_{SC} of 24.0 mA cm^{-2}, V_{OC} of 1.03 V and an impressive FF of 84.5%. Finally, the reference device containing **Me-4PACz**, as expected, achieved the highest device performance, obtaining a PCE of 23.2%, with 24.7 mA cm^{-2} J_{SC}, a V_{OC} of 1.13 V, and a FF of 82.9%.

The statistical distribution of the photovoltaic parameters of all devices tested can be seen in Fig. S16. The improvements observed in devices utilising **Spiro-B**, when compared to **Spiro-A**, mainly arise from an increase in V_{OC} and FF. Reference devices containing **Me-4PACz**, however, outperform both **Spiro-A** and **Spiro-B** across all parameters on average, as seen in Fig. S16. Furthermore, we note that minimal to non-existent hysteresis is present for all devices studied here.

Charge carrier dynamics *via* time-resolved photoluminescence

To understand where the variation in device performance originates, we employ time-resolved photoluminescence (TRPL) spectroscopy. The decay transients obtained from perovskite on ITO, which has been treated with **Spiro-A** and **Spiro-B**, are shown in Fig. 3b. To analyse the TRPL data, we employ a rate equation based on a bimolecular-trapping-Auger model that accounts for the different possible competing processes.[25] The extracted parameters obtained from the rate equation can be found in SI Table S2, and further discussion on the rate equation is in SI Note 2.

It can be seen from the analysis that both Spiro derivatives have a rapid initial decay. This is surprising, as **Me-4PACz** is known to extend monomolecular lifetimes well beyond what was obtained for the Spiro derivatives.[26,27] However, performance remained high for both **Spiro-A** and **Spiro-B**. This raises a question: Why does **Me-4PACz** outperform the Spiro derivatives? One would expect *a priori* that faster decay may indicate faster charge extraction.

As the Spiro moieties follow inspiration from the dye-sensitised solar cell design principles, we postulate that, for **Spiro-A** and **Spiro-B**, charge injection will occur through the SAM layer.[28] This explains why the photoluminescence decay dynamics of these materials are much faster than those of the reference carbazole, **Me-4PACz**. The initial rapid decay observed in the Spiro moieties could suggest that a significant fraction of photogenerated charge may undergo rapid interfacial recombination rather than accumulate in the perovskite. As a result, quasi-Fermi level splitting (QFLS) would be reduced, resulting in a lower V_{OC} when compared to **Me-4PACz**, as observed in the device *J*–*V* performance.

However, it can be observed that the decay of **Spiro-A** is longer than that of the **Spiro-B** sample, despite **Spiro-B**

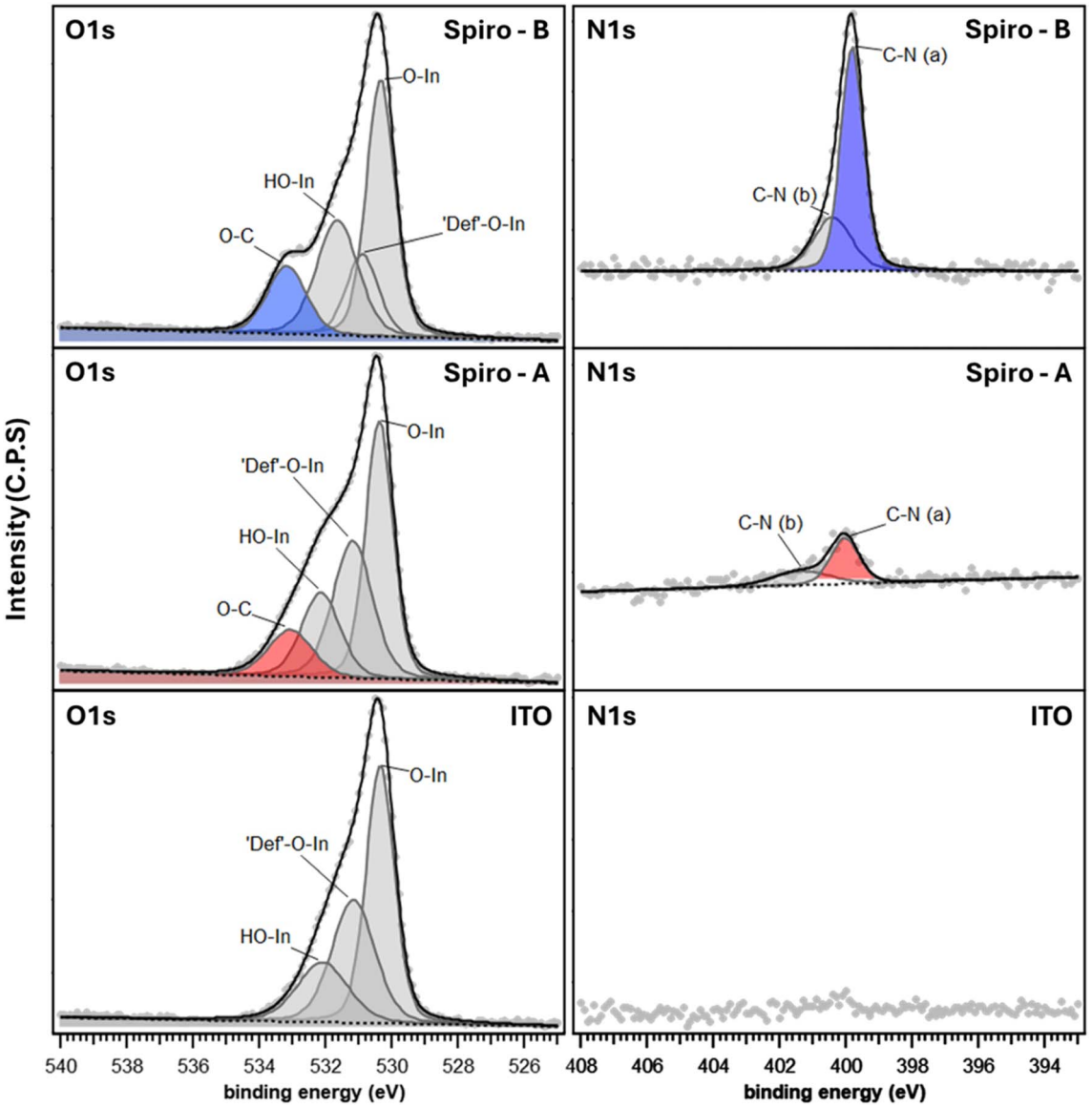

Fig. 2 O 1s and N 1s XPS spectra of ITO coated with **Spiro-A**, **Spiro-B**, or without. Here, the peaks relating to the ITO substrate are greyed out. Peaks relating to the presence of **Spiro-A** are highlighted in red, and peaks relating to the presence of **Spiro-B** are highlighted in blue for clarity.

obtaining a higher V_{OC}. This result is seemingly counterintuitive; to investigate this, we employ the differential lifetime method to gain a deeper understanding of the interface dynamics.[29] The resulting plot is shown in Fig. S17. From this, we can see that the Spiro derivatives have similar extraction capabilities as the dynamics are very similar at early lifetimes. However, **Spiro-B** has a longer differential lifetime compared to **Spiro-A** at later times. This indicates that despite the initial rapid decay, **Spiro-B** may have reduced surface recombination compared to **Spiro-A**. This would result in additional charge accumulation and ultimately lead to a slightly higher V_{OC}. This is supported by the analysis carried out using the rate equation (full details in Table S2), which shows that **Spiro-A** has a slightly higher percentage of monomolecular recombination (k_1) compared to **Spiro-B**.

Stabilise and pulse (SaP) measurements: probing built-in potential and recombination

We note here that the TRPL measurements are conducted on half-cells. Therefore, we are not probing the dynamics that would be present in a complete device.[25] This is in part due to the lack of a complete circuit and the subsequent electric field that would form, which critically impacts photogenerated charge accumulation and extraction.[30] To overcome this, we utilise the stabilise and pulse (SaP) technique.[31] This measurement is performed on complete working devices and examines the effect of ionic field screening on charge extraction, providing clear insights into how different charge extraction layers influence recombination and extraction.[14] We have previously used the SaP technique to probe how device

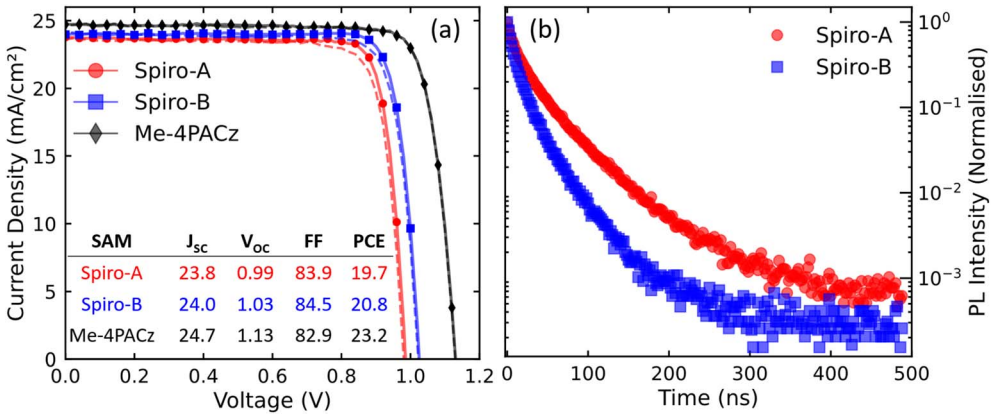

Fig. 3 (a) Current density–voltage (J–V) curves of champion devices incorporating **Spiro-A**, **Spiro-B** and **Me-4PACz**. Inset as a table are the champion device parameters, including short-circuit current density (mA cm^{-2}), open-circuit voltage (V), fill factor (%) and power conversion efficiency (%). Reverse scans are shown as solid lines with markers, and the forward scans as dashed lines. (b) Normalised time-resolved photoluminescence (TRPL) data for perovskite films deposited on ITO/SAM substrates.

energetics change when using different carbazole-based SAMs.[14] A more in-depth discussion of the measurement details is provided in previous works.[14,30,31]

The full reconstructed J–V curves obtained under 1 Sun conditions across a range of stabilisation voltages for representative devices of **Spiro-A**, **Spiro-B** and **Me-4PACz** are shown in Fig. 4. The individual analysis for each SaP measurement can be found in Fig. S18. All associated stabilisation data obtained during the measurement can be found in Fig. S19, demonstrating that all devices had reached a steady current output before initiating the pulsing sequence.

Interestingly, we observe significant differences in the J–V curve depending on ionic motion, even though all studied devices showed little to no hysteresis during the traditional J–V sweep (see Fig. 3). This is an important point, as it is a common belief that a lack of observable hysteresis implies suppressed ionic motion. However, previous works have discussed in detail why this is not the case.[32,33] Although for this measurement, we note that for each stabilisation voltage, a forward and reverse scan was conducted, and no hysteresis was present, as shown in Fig. S20. As we are holding the ions in position, then in this instance, no hysteresis acts as an additional indicator that ions remain at quasi steady-state during the measurement.

By analysing the change in gradient around the open circuit voltage ($dJ/dV|_{V=V_{oc}}$) for each J–V curve obtained, we can extract the flat band potential (V_{Flat}), as shown in Fig. 5a. This value is proportional to the built-in potential in PSCs.[30] For more information on how this value is extracted, see the Methods section and ref. 14. From this analysis, we can make two clear observations: (i) there is a significant shift in the V_{Flat} with **Spiro-B** yielding a much lower value, and (ii) the slope of the curve for **Spiro-B** is significantly shallower compared to both

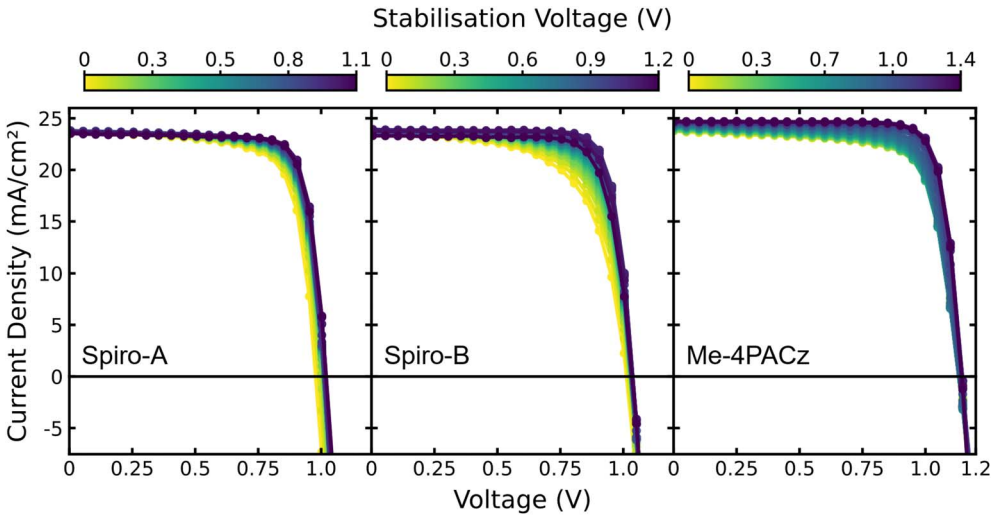

Fig. 4 Full reconstructed stabilise and pulse J–Vs across a range of stabilisation voltages for devices containing **Spiro-A**, **Spiro-B** and **Me-4PACz**. In all graphs, yellow indicates low stabilisation voltages and purple indicates high stabilisation voltages, as displayed in the corresponding colour bars above each graph.

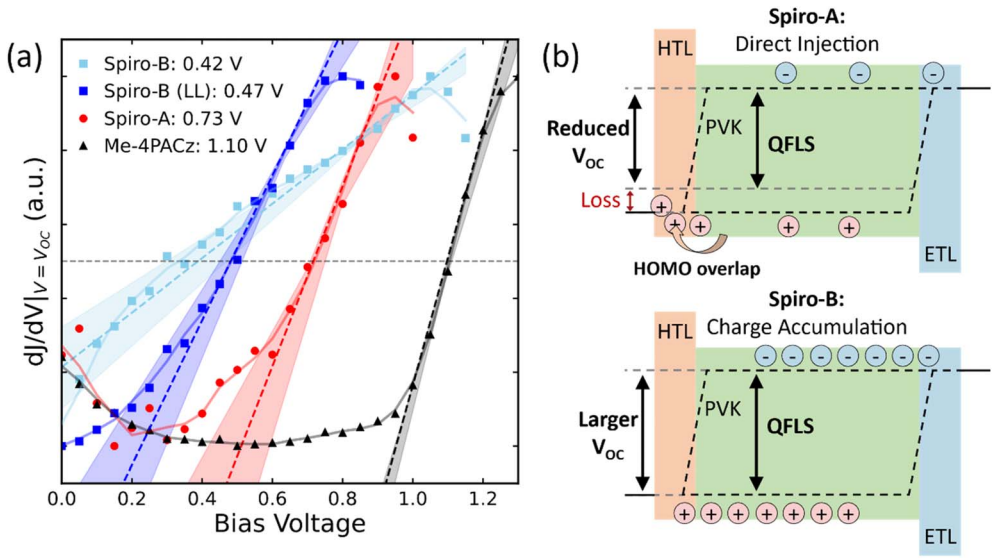

Fig. 5 (a) Normalised gradient analysis around open circuit voltage ($dJ/dV|_{V=V_{oc}}$) from the SaP data obtained for all samples. In this figure, all data points are shown by markers and a Savitzky–Golay smoothing filter is included as a lighter shaded solid line behind as a guide to the eye. The midpoint of the maxima and minima is shown as a grey horizontal dashed line, and finally, an example of one fit used to obtain the V_{Flat} value is shown as a dashed line, the same colour as the marker for clarity. The range of fits used to obtain the V_{Flat} value is shown as a lighter shaded region. The light blue **Spiro-B** (LL) refers to the low light measurement (~0.3 Suns), whereas the dark blue **Spiro-B** is the regular 1 Sun measurement. (b) Cartoon schematic of the difference in quasi-Fermi level splitting (QFLS) in devices using **Spiro-A** and **Spiro-B**. Here, the HOMO overlap of the **Spiro-A** reduces the QFLS in the perovskite compared to devices using **Spiro-B**.

Spiro-A and the **Me-4PACz** reference. Here, the latter point is likely caused by the former. Where the lower V_{Flat} likely indicates greater overlap between electron and hole populations,[30] which increases bulk recombination, as reflected in the data.

Charge accumulation *vs.* extraction: mechanistic insights

A change in V_{Flat} directly reflects a shift in device energetics, as this measurement probes the Fermi levels of the transport layers adjacent to the perovskite. The extracted values of 0.42 ± 0.10 V for **Spiro-B**, 0.73 ± 0.05 V for **Spiro-A** and 1.10 ± 0.05 V for **Me-4PACz** confirm that the SAM used strongly influences energetics. This is despite the fact that the Spiro derivatives exhibit similar HOMO levels as measured through CV. This difference can be explained by the molecular dipole moments obtained by DFT. **Spiro-A** was found to have a large dipole (~8.1 D), while **Spiro-B** is significantly lower (~2.9 D). A stronger dipole will induce a greater shift in the ITO work function, thereby increasing the V_{Flat}.[34]

It is surprising here that the conventional approach of maximising the HOMO level overlap with the charge extraction contact, both energetically and spatially, actually delivers the worst results of the set. Based on our previous work, one would expect *a priori* that a larger V_{Flat} would yield a higher V_{OC}, as was observed for a set of SAM layers with different substituents, which systematically increased the dipole from 0.2 to 2 D, yielding an improvement in open circuit voltage from 1.07 to 1.09 V.[14] Yet, this does not seem to be the case here. **Spiro-B**, despite exhibiting a much lower V_{Flat}, actually obtained a higher V_{OC}.

It is worth restating here that the V_{OC} of a perovskite solar cell is directly proportional to the QFLS[35,36] within the perovskite film for a given illumination intensity, where higher charge density leads to a higher QFLS.[12,37,38] Effectively, there are two competing effects impacting the open circuit voltage for **Spiro-A**. Its HOMO level configuration funnels charge efficiently out of the device, which reduces the charge density in the perovskite (as intended); however, this reduces the QFLS and therefore the V_{OC}. Secondly, raising the dipole strength leads to a higher V_{Flat}, which reduces the electron and hole overlap, resulting in decreased recombination (*i.e.*, less charge is lost).[30] This would normally lead to an increase in the QFLS. However, it is clear for **Spiro-A** that the charge extraction funnel is the dominating factor, explaining the observed V_{OC} loss for these devices. Conversely, in a device where this extraction channel is blocked or hindered, as is expected for **Spiro-B** with its spatially separated HOMO level, this will lead to additional charge accumulation in the device, thus increasing the QFLS. This is shown in the cartoon diagram Fig. 5b, where it can be seen that **Spiro-B** can accumulate more charge, increasing the relative QFLS.

We have established previously that **Me-4PACz** induces a slight energetic barrier at the interface, leading to significant charge accumulation and a correspondingly increased V_{OC}.[14] This is consistent with the results obtained here, where, again, **Me-4PACz** leads to the highest open-circuit voltage. Interestingly, this work conclusively demonstrates that the HOMO level of the SAM molecule, as estimated by CV, plays only a minor role in the built-in potential of the device. In this device architecture, this parameter is primarily determined by the dipole

strength of the anchored molecule, where a stronger dipole results in an increased built-in potential.[14]

This finding shows that focusing only on energy level alignment may lead to performance loss. However, if injection is prevented by synthetically modifying the molecule to include a physical spacer between the HOMO and the charge extraction contact, performance can be partly recovered even in a device with a low built-in potential. This result significantly influences researchers working on designing new transport layers, shifting the focus to how a material affects device energetics when attached to a surface rather than solely optimising energy alignment based on conduction/valence band positions.

Conclusion

This study provides compelling evidence that efficient charge injection through self-assembled molecules is not necessarily the optimal approach for enhancing perovskite solar cell performance. To demonstrate this, we have synthesised two spiro-derivatives: **Spiro-A** and **Spiro-B**. **Spiro-A** is directly attached to the ITO anode by a carboxylic acid moiety, forcing the HOMO level to be in close proximity to the ITO. In contrast, **Spiro-B** incorporates a spacer group to separate the HOMO from the ITO spatially. When incorporated in PSCs, **Spiro-B** achieves a higher V_{OC} and PCE than **Spiro-A**, even though both molecules exhibit nearly identical energy level alignment as estimated *via* cyclic voltammetry and light absorption measurements. To explain these differences, we performed stabilise and pulse measurements. Our results show that **Spiro-A** exhibits a greater built-in potential than **Spiro-B**, consistent with its stronger dipole moment, which one would expect to lead to a higher V_{OC}.

Here, we propose that **Spiro-A**'s HOMO overlap with the ITO will promote efficient charge extraction, thus reducing photogenerated charge carrier density across the whole device. In contrast, **Spiro-B**, which lacks the HOMO overlap due to the alkyl spacer, results in increased QFLS, leading to an improved V_{OC} and consequently a PCE increase. Nevertheless, it is essential to note here that the reference SAM, **Me-4PACz**, outperforms both Spiro derivatives in all metrics, emphasising the significance of controlled interfacial recombination and charge accumulation in improving quasi-Fermi level splitting. These findings challenge the conventional focus on maximising charge injection efficiency and highlight the importance of balancing interfacial energy barriers, dipole strength, and recombination dynamics in SAM design to optimise device performance.

Author contributions

F. J. A. and L. M. contributed to this work equally. F. J. A. wrote the manuscript. F. J. A. and P. D. conceived the experiments for the characterisation. L. M. and G. C. designed and synthesised the molecule. D. W. and L. M. performed the characterisation of the new material under the supervision of G. C. W. L. and E. P. fabricated the devices, carried out solar cell characterisations and conducted device data discussions. F. J. A. performed the stabilise and pulse measurements and interpreted the results under the supervision of P. D. M. G. performed the XPS measurements and interpreted the results under the supervision of P. D. and E. A. All authors participated in discussing the results, manuscript writing and approved the final submission.

Conflicts of interest

There are no conflicts to declare.

Data availability

Data used to generate the main-text figures in this article are available at **https://doi.org/10.5281/zenodo.15544593**. Additional supporting data are provided in the supplementary information (SI). Supplementary information: complete synthetic procedure for **Spiro-B**. Additional characterisation of **Spiro-B**. Note on TRPL analysis. XPS spectra of all materials used and a table of associated data. Complete device parameters obtained from *J–V* characterisation. Stabilise and pulse measurement, V_{Flat} analysis and stabilisation data from SaP measurement for all devices. See DOI: **https://doi.org/10.1039/d5ta06749a**.

Acknowledgements

For this work, F. J. A. and M. G. gratefully acknowledge the University of Glasgow for financial support for this research through the School of Chemistry scholarships. P. D., F. J. A., and M. G. thank the EPSRC for funding through grants EP/T010569/1 and EP/T517896/1. The work carried out by W. L. is supported by the Spanish Government and AGAUR (PID2019-109389RB-I00 and 2021 SGR 01261, respectively). We also acknowledge the Severo Ochoa grant MCIN/AEI/10.13039/501100011033 (CEX2019-000925-S). W. L. thanks the MSCA-COFUND I2: ICIQ Impulsion (GA 801474) for support. W. L. thanks Dr Eugenia Martínez-Ferrero for the results discussions. E. P. also acknowledges ICIQ, CERCA, and ICREA for financial support. G. C. thanks the Leverhulme Trust for a Research Fellowship. G. C., L. M., and D. W. gratefully acknowledge support from the EPSRC for funding through grants EP/V027425/1, EP/E036244/1, EP/T517896/1 and EP/N509668/1. E. A. acknowledges support by the Engineering and Physical Sciences Research Council (EP/X032116/1).

References

1 Y. Yang, H. Chen, C. Liu, J. Xu, C. Huang, C. D. Malliakas, H. Wan, A. S. R. Bati, Z. Wang, R. P. Reynolds, I. W. Gilley, S. Kitade, T. E. Wiggins, S. Zeiske, S. Suragtkhuu, M. Batmunkh, L. X. Chen, B. Chen, M. G. Kanatzidis and E. H. Sargent, *Science*, 2024, **386**, 898–902.
2 M. M. Lee, J. Teuscher, T. Miyasaka, T. N. Murakami and H. J. Snaith, *Science*, 2012, **338**, 643–647.
3 H. Zhou, Q. Chen, G. Li, S. Luo, T. Song, H.-S. Duan, Z. Hong, J. You, Y. Liu and Y. Yang, *Science*, 2014, **345**, 542–546.
4 A. Abrusci, S. D. Stranks, P. Docampo, H.-L. Yip, A. K.-Y. Jen and H. J. Snaith, *Nano Lett.*, 2013, **13**, 3124–3128.

5 G. Yang, C. Wang, H. Lei, X. Zheng, P. Qin, L. Xiong, X. Zhao, Y. Yan and G. Fang, *J. Mater. Chem. A*, 2017, **5**, 1658–1666.
6 Z. Dai, S. K. Yadavalli, M. Chen, A. Abbaspourtamijani, Y. Qi and N. P. Padture, *Science*, 2021, **372**, 618–622.
7 H. Tang, Z. Shen, Y. Shen, G. Yan, Y. Wang, Q. Han and L. Han, *Science*, 2024, **383**, 1236–1240.
8 X. Lin, A. N. Jumabekov, N. N. Lal, A. R. Pascoe, D. E. Gómez, N. W. Duffy, A. S. R. Chesman, K. Sears, M. Fournier, Y. Zhang, Q. Bao, Y.-B. Cheng, L. Spiccia and U. Bach, *Nat. Commun.*, 2017, **8**, 613.
9 A. Al-Ashouri, A. Magomedov, M. Roß, M. Jošt, M. Talaikis, G. Chistiakova, T. Bertram, J. A. Márquez, E. Köhnen, E. Kasparavičius, S. Levcenco, L. Gil-Escrig, C. J. Hages, R. Schlatmann, B. Rech, T. Malinauskas, T. Unold, C. A. Kaufmann, L. Korte, G. Niaura, V. Getautis and S. Albrecht, *Energy Environ. Sci.*, 2019, **12**, 3356–3369.
10 Y. Peng, Y. Chen, J. Zhou, C. Luo, W. Tang, Y. Duan, Y. Wu and Q. Peng, *Nat. Commun.*, 2025, **16**, 1252.
11 X. Zheng, Z. Li, Y. Zhang, M. Chen, T. Liu, C. Xiao, D. Gao, J. B. Patel, D. Kuciauskas, A. Magomedov, R. A. Scheidt, X. Wang, S. P. Harvey, Z. Dai, C. Zhang, D. Morales, H. Pruett, B. M. Wieliczka, A. R. Kirmani, N. P. Padture, K. R. Graham, Y. Yan, M. K. Nazeeruddin, M. D. McGehee, Z. Zhu and J. M. Luther, *Nat. Energy*, 2023, **8**, 462–472.
12 H. Chen, A. Maxwell, C. Li, S. Teale, B. Chen, T. Zhu, E. Ugur, G. Harrison, L. Grater, J. Wang, Z. Wang, L. Zeng, S. M. Park, L. Chen, P. Serles, R. A. Awni, B. Subedi, X. Zheng, C. Xiao, N. J. Podraza, T. Filleter, C. Liu, Y. Yang, J. M. Luther, S. De Wolf, M. G. Kanatzidis, Y. Yan and E. H. Sargent, *Nature*, 2023, **613**, 676–681.
13 J. Siekmann, A. Kulkarni, S. Akel, B. Klingebiel, M. Saliba, U. Rau and T. Kirchartz, *Adv. Energy Mater.*, 2023, **13**, 2300448.
14 F. J. Angus, W. K. Yiu, H. Mo, T. L. Leung, M. U. Ali, Y. Li, J. Wang, A. W. Y. Ho-Baillie, G. Cooke, A. B. Djurišić and P. Docampo, *J. Phys. Chem. Lett.*, 2024, **15**, 10686–10695.
15 Z. Li, X. Sun, X. Zheng, B. Li, D. Gao, S. Zhang, X. Wu, S. Li, J. Gong, J. M. Luther, Z. Li and Z. Zhu, *Science*, 2023, **382**, 284–289.
16 S. Zhang, F. Ye, X. Wang, R. Chen, H. Zhang, L. Zhan, X. Jiang, Y. Li, X. Ji, S. Liu, M. Yu, F. Yu, Y. Zhang, R. Wu, Z. Liu, Z. Ning, D. Neher, L. Han, Y. Lin, H. Tian, W. Chen, M. Stolterfoht, L. Zhang, W.-H. Zhu and Y. Wu, *Science*, 2023, **380**, 404–409.
17 S. Wooh, T.-Y. Kim, D. Song, Y.-G. Lee, T. K. Lee, V. W. Bergmann, S. A. L. Weber, J. Bisquert, Y. S. Kang and K. Char, *ACS Appl. Mater. Interfaces*, 2015, **7**, 25741–25747.
18 X. Yang, S. Zhang, K. Zhang, J. Liu, C. Qin, H. Chen, A. Islam and L. Han, *Energy Environ. Sci.*, 2013, **6**, 3637–3645.
19 E. Ghadiri, S. M. Zakeeruddin, A. Hagfeldt, M. Grätzel and J.-E. Moser, *Sci. Rep.*, 2016, **6**, 24465.
20 L. Zhang, L. Favereau, Y. Farré, E. Mijangos, Y. Pellegrin, E. Blart, F. Odobel and L. Hammarström, *Phys. Chem. Chem. Phys.*, 2016, **18**, 18515–18527.
21 L. J. Antila, P. Myllyperkiö, S. Mustalahti, H. Lehtivuori and J. Korppi-Tommola, *J. Phys. Chem. C*, 2014, **118**, 7772–7780.
22 M. Cariello, N. Pant, A. H. Harkiss, F. M. Tracey, J. Cameron, P. J. Skabara, P. J. Holliman, P. Docampo and G. Cooke, *Mol. Syst. Des. Eng.*, 2022, **7**, 899–905.
23 C. Donley, D. Dunphy, D. Paine, C. Carter, K. Nebesny, P. Lee, D. Alloway and N. R. Armstrong, *Langmuir*, 2002, **18**, 450–457.
24 L. Basta, A. Moscardini, F. Fabbri, L. Bellucci, V. Tozzini, S. Rubini, A. Griesi, M. Gemmi, S. Heun and S. Veronesi, *Nanoscale Adv.*, 2021, **3**, 5841–5852.
25 L. Krückemeier, B. Krogmeier, Z. Liu, U. Rau and T. Kirchartz, *Adv. Energy Mater.*, 2021, **11**, 2003489.
26 A. Al-Ashouri, E. Köhnen, B. Li, A. Magomedov, H. Hempel, P. Caprioglio, J. A. Márquez, A. B. Morales Vilches, E. Kasparavicius, J. A. Smith, N. Phung, D. Menzel, M. Grischek, L. Kegelmann, D. Skroblin, C. Gollwitzer, T. Malinauskas, M. Jošt, G. Matič, B. Rech, R. Schlatmann, M. Topič, L. Korte, A. Abate, B. Stannowski, D. Neher, M. Stolterfoht, T. Unold, V. Getautis and S. Albrecht, *Science*, 2020, **370**, 1300–1309.
27 Y. Yuan, G. Yan, C. Dreessen, T. Rudolph, M. Hülsbeck, B. Klingebiel, J. Ye, U. Rau and T. Kirchartz, *Nat. Mater.*, 2024, **23**, 391–397.
28 S. E. Koops, B. C. O'Regan, P. R. F. Barnes and J. R. Durrant, *J. Am. Chem. Soc.*, 2009, **131**, 4808–4818.
29 B. Krogmeier, F. Staub, D. Grabowski, U. Rau and T. Kirchartz, *Sustainable Energy Fuels*, 2018, **2**, 1027–1034.
30 L. J. F. Hart, F. J. Angus, Y. Li, A. Khaleed, P. Calado, J. R. Durrant, A. B. Djurišić, P. Docampo and P. R. F. Barnes, *Energy Environ. Sci.*, 2024, **17**, 7107–7118.
31 N. S. Hill, M. V. Cowley, N. Gluck, M. H. Fsadni, W. Clarke, Y. Hu, M. J. Wolf, N. Healy, M. Freitag, T. J. Penfold, G. Richardson, A. B. Walker, P. J. Cameron and P. Docampo, *Adv. Mater.*, 2023, **35**, 2302146.
32 G. Richardson, S. E. J. O'Kane, R. G. Niemann, T. A. Peltola, J. M. Foster, P. J. Cameron and A. B. Walker, *Energy Environ. Sci.*, 2016, **9**, 1476–1485.
33 P. Calado, A. M. Telford, D. Bryant, X. Li, J. Nelson, B. C. O'Regan and P. R. F. Barnes, *Nat. Commun.*, 2016, **7**, 13831.
34 Q. Chen, C. Wang, Y. Li and L. Chen, *J. Am. Chem. Soc.*, 2020, **142**, 18281–18292.
35 P. Caprioglio, M. Stolterfoht, C. M. Wolff, T. Unold, B. Rech, S. Albrecht and D. Neher, *Adv. Energy Mater.*, 2019, **9**, 1901631.
36 J. Warby, S. Shah, J. Thiesbrummel, E. Gutierrez-Partida, H. Lai, B. Alebachew, M. Grischek, F. Yang, F. Lang, S. Albrecht, F. Fu, D. Neher and M. Stolterfoht, *Adv. Energy Mater.*, 2023, **13**, 2303135.
37 W. Xu, L. J. F. Hart, B. Moss, P. Caprioglio, T. J. Macdonald, F. Furlan, J. Panidi, R. D. J. Oliver, R. A. Pacalaj, M. Heeney, N. Gasparini, H. J. Snaith, P. R. F. Barnes and J. R. Durrant, *Adv. Energy Mater.*, 2023, **13**, 2301102.
38 M. Stolterfoht, P. Caprioglio, C. M. Wolff, J. A. Márquez, J. Nordmann, S. Zhang, D. Rothhardt, U. Hörmann, Y. Amir, A. Redinger, L. Kegelmann, F. Zu, S. Albrecht, N. Koch, T. Kirchartz, M. Saliba, T. Unold and D. Neher, *Energy Environ. Sci.*, 2019, **12**, 2778–2788.

